

This is the author's final, peer-reviewed manuscript as accepted for publication (AAM). The version presented here may differ from the published version, or version of record, available through the publisher's website. This version does not track changes, errata, or withdrawals on the publisher's site.

Structure and spectroscopy of the supercapacitor material hydrous ruthenium oxide, $\text{RuO}_2 \cdot x\text{H}_2\text{O}$, by neutron scattering

Stewart F Parker, Stephen J. Robertson and Silvia Imberti

Published version information

Citation: SF Parker, SJ Robertson and S Imberti. "Structure and spectroscopy of the supercapacitor material hydrous ruthenium oxide, $\text{RuO}_2 \cdot x\text{H}_2\text{O}$, by neutron scattering." *Molecular Physics*, Soper Special Issue (2019).

DOI: [10.1080/00268976.2019.1649491](https://doi.org/10.1080/00268976.2019.1649491)

This is an Accepted Manuscript of an article published by Taylor & Francis in Molecular Physics on 01-08-19, available online: <http://www.tandfonline.com/>

This version is made available in accordance with publisher policies. Please cite only the published version using the reference above. This is the citation assigned by the publisher at the time of issuing the AAM/APV. Please check the publisher's website for any updates.

This item was retrieved from **ePubs**, the Open Access archive of the Science and Technology Facilities Council, UK. Please contact epubs@stfc.ac.uk or go to <http://epubs.stfc.ac.uk/> for further information and policies.

Structure and spectroscopy of the supercapacitor material hydrous ruthenium oxide, $\text{RuO}_2 \cdot x\text{H}_2\text{O}$, by neutron scattering

Stewart F Parker^{a*} Stephen J. Robertson^b and Silvia Imberti^a

^a*ISIS Facility, STFC Rutherford Appleton Laboratory, Chilton, Didcot, OX11 0QX, UK*

^b*Advanced Material Group, STFC Rutherford Appleton Laboratory, Chilton, Didcot, Oxfordshire, OX11 0QX, UK*

E-mail: stewart.parker@stfc.ac.uk

Dedicated to Professor Alan Soper FRS on the occasion of his retirement.

SFP ORCID id: 0000-0002-3228-2570

SI ORCID id: 0000-0001-7037-6829

Word count = 4004

Structure and spectroscopy of the supercapacitor material $\text{RuO}_2 \cdot x\text{H}_2\text{O}$ by neutron scattering

Hydrous ruthenium dioxide, $\text{RuO}_2 \cdot x\text{H}_2\text{O}$, is a material of active investigation as an electrode material for supercapacitors. A combination of elastic and inelastic neutron scattering together with thermal gravimetric studies and DFT calculations have provided new insight into the nature of the surface species present on $\text{RuO}_2 \cdot x\text{H}_2\text{O}$. Our results confirm that hydrous ruthenium oxide is a nanocrystalline material consisting of a core of RuO_2 . We show that the surface consists largely of Ru–OH with small amounts of water hydrogen-bonded to the surface. The hydroxyls are stable up to ~ 200 °C, *i.e.* over the composition range $x = 0.2 - 2$. The optimal supercapacitor material has $x = 0.5 - 0.7$, and in this range the surface is fully hydroxylated. This provides a route for the proton transport: a proton can attach to a surface hydroxyl to generate coordinated water, proton transport then occurs along the hydrogen-bonded chain by a Grotthuss mechanism.

Keywords: hydrous ruthenium oxide; neutron diffraction; inelastic neutron scattering spectroscopy; thermal gravimetric analysis; density functional theory

Introduction

Supercapacitors (also called electric double-layer capacitors or ultracapacitors) are energy storage devices with very high capacity and a low internal resistance [1-3]. Some of the benefits of supercapacitors when compared with other energy storage devices are: long life, high power, flexible packaging, wide thermal range (-40 °C to 70 °C), low maintenance and low weight [4]. Supercapacitors are best be utilized in areas that require applications with short load cycle and high reliability, such as forklifts, load cranes and as energy storage to smooth load-demand cycles for electric utilities and as backup power supplies. Supercapacitors can also supplement fuel cells in electric vehicles and low emission hybrids [5].

A supercapacitor consists of two electrodes, an electrolyte, and a separator which isolates the two electrodes electrically. The mechanism of energy storage is a simple charge separation at the interface between the electrode and the electrolyte. The key component is the electrode material. Typically, this is a high surface area activated carbon [6]. Metal oxides have also been used and the best of these is hydrous ruthenium dioxide, $\text{RuO}_2 \cdot x\text{H}_2\text{O}$, $x \sim 2$ [7-11]. To reduce the cost, $\text{RuO}_2 \cdot x\text{H}_2\text{O}$ doped carbons have been extensively investigated [12,13]. The material is also of interest in polymer electrolyte membrane fuel cells [14,15] and as a catalyst [16,17].

Hydrous ruthenium dioxide has been investigated by a variety of techniques including, electron microscopy [18], X-ray spectroscopies [19], X-ray pdf analysis [20,21] and NMR [22]. The structural studies [18-21] show that ruthenium is sixfold coordinated and is present as RuO_6 units. The pdf analysis concluded that “ $\text{RuO}_2 \cdot x\text{H}_2\text{O}$ is a composite of anhydrous rutile-like RuO_2 nanocrystals dispersed by boundaries of structural water associated with Ru-O” [20,21]. The NMR study [22] showed that the water is mobile to as low a temperature as 213 K and that the hydrogen bonding between the water and the ruthenium oxide varies with the water content. Thus while the state of the ruthenium oxide is reasonably well understood, how the water interacts with the oxide is not clear. This is because the structural studies are dominated by the ruthenium ions (because the scattering strength of an atom to electrons or X-rays directly depends on its atomic number) and not to the water. The NMR studies give information on the proton motion but only indirectly on the state of the hydrogen; *i.e.* whether it is present as hydroxyl, water or hydroxonium.

In contrast, neutrons are strongly scattered by hydrogen and the use of neutron techniques enables a complementary view of hydrous ruthenium oxide. In this work we use both structural (total neutron scattering) and spectroscopic (inelastic neutron

scattering, INS) probes to provide new insights into this material as a function of water content.

Experimental

Hydrous ruthenium dioxide powder, $\text{RuO}_2 \cdot x\text{H}_2\text{O}$ (Alfa Aesar) was used as received. The water content was adjusted by heating in air at selected temperatures [20] in an oven overnight. After preparation the samples were loaded into indium wire-sealed cans as quickly as possible. Our experience is that such cans are sufficiently well sealed that even very air sensitive materials are stable for days, much longer than the time needed for the neutron scattering measurements.

The water content was determined analytically by the weight loss and by thermogravimetric analysis (TGA, Perkin-Elmer Pyris 1, Ar purge gas at $20 \text{ cm}^3 \text{ min}^{-1}$ and ramped at $5 \text{ }^\circ \text{ min}^{-1}$ from 50 to $800 \text{ }^\circ \text{C}$). Particularly for the larger values of x , this is a lower bound, since it was losing water immediately on loading into the TGA apparatus. The gravimetric values are more reliable and are those used throughout the remainder of the paper. Table 1 summarises the samples used.

The neutron experiments were performed at the ISIS spallation neutron source, located at the STFC Rutherford Appleton Laboratory (United Kingdom). The room temperature total scattering neutron measurements used the SANDALS diffractometer. SANDALS is a diffractometer optimized for the study of liquids and amorphous samples containing light elements. The standard corrections and normalizations have been applied to the data through the set of programs gathered under the graphical interface GudrunN. The theoretical background to the operations performed by the program are described elsewhere [23].

The physical quantity measured by the diffractometer is the differential scattering cross section $d\sigma/d\Omega$ as a function of the exchanged wave vector Q (defined as

the modulus of the difference between the incident and the scattered neutron wave vectors). Through the basic theory of neutron scattering, it is possible to relate this quantity to the static structure factor, $F(Q)$, which is the Fourier transform of the atomic pair distribution function, $g(r)$. The latter contains the information about the correlation between the positions of two atoms in the system at a given moment in time.

The neutron vibrational spectroscopy (inelastic neutron scattering, INS) measurements were carried out with TOSCA [24] and MAPS [25]. To minimise the Debye-Waller factor, the spectra were recorded <20 K.

Periodic DFT calculations were carried out using the plane-wave pseudopotential method as implemented in the CASTEP code [26]. Exchange and correlation were approximated using the Perdew-Burke-Ernzerhof (PBE) functional [27], within the generalized gradient approximation (GGA). Norm-conserving pseudopotentials were generated using the kinetic-energy optimised method [28] with a plane-wave cut-off energy of 830 eV. The equilibrium structure, an essential prerequisite for lattice dynamics calculations was obtained by Broyden-Fletcher-Goldfarb-Shanno (BFGS) geometry optimization after which the residual forces were typically converged to zero within ± 0.005 eV \AA^{-1} . Phonon frequencies were obtained by diagonalization of dynamical matrices computed using density-functional perturbation theory [29] (DFPT). For this purpose, dynamical matrices were computed on a regular grid of wavevectors throughout the Brillouin zone and Fourier interpolation was used to extend the computed grid to the desired fine set of points along the high-symmetry paths. The INS spectra were generated from the CASTEP output using ACLIMAX [30].

Results and discussion

Figure 1a-d shows the neutron diffraction patterns for samples that span the entire range

of water contents. Comparison of the diffraction pattern of the material dried at 500 °C with that of authentic anhydrous RuO₂, Figure 1e, confirms the assignment [20,21] as the rutile form of RuO₂. However, the hydrated samples, Figure 1a-c, do show the main features present in the crystalline material. The corresponding radial distribution functions are shown in Figure 2. It should be noted that all the experiments (INS, diffraction and TGA) used protonated material. ¹H has a negative scattering length, while oxygen (and ruthenium) have positive scattering lengths, thus the oxygen-to-hydrogen correlation results in a negative-going peak (*i.e.* $- \times + = -$). It is apparent that as the drying temperature is increased, the number of OH-containing species decreases (the negative peak at $\sim 1 \text{ \AA}$) as expected. Together, Figures 1 and 2 confirm that RuO₂.*x*H₂O is nanocrystalline and that the crystallinity increases with increasing drying temperature, as shown by the increased persistence of the oscillations beyond 5 Å in Figure 2.

Figure 3 shows the INS spectra of RuO₂.*x*H₂O for a range of water contents. Comparison of the spectrum of the ‘as received’ sample with $x = 2.02 \text{ H}_2\text{O}$, Figure 3b, with that of ice I_h, Figure 3a, shows that the distinct features of the latter assigned to the translational optic modes [31] at 100 – 350 cm⁻¹ have been replaced by a continuum and the sharp ‘cliff edge’ of the librational modes at 540 cm⁻¹ is broadened and shifted to lower energy. These are all features characteristic of disordered water and are commonly seen for water on metal oxide surfaces *e.g.* [32–34]. This is confirmed by the spectrum in the O–H stretch region, Figure 4, which in comparison to ice I_h, 4a, shows the stretch modes broadened and shifted to higher transition energy, 4b, consistent with weaker hydrogen bonding than in ice I_h.

Drying RuO₂.*x*H₂O to progressively higher temperature, in the range 100 – 190 °C, generates materials with $0.99 \geq x \geq 0.46$. The spectra of these are remarkably

similar: the onset of the librational modes has downshifted slightly to 340 cm^{-1} from 360 cm^{-1} in the $x = 2.02$ sample, showing a further weakening of the water hydrogen bonding network. The peak maximum shifts from 560 cm^{-1} in Figure 3b to 470 cm^{-1} in Figure 3c-f. A distinct peak is also apparent at 935 cm^{-1} , which by comparison to the results from an experimental and DFT study of hydrous palladium oxide [32] and activated alumina, where only hydroxyls are present [35], is assigned to the Ru–O–H bending mode of a surface hydroxyl.

As the water content is further reduced to $x = 0.12$, Figure 3g, the intensity of the water librational modes is further reduced. This is consistent with the residual water being much more strongly hydrogen bonded. It is definitely water and not a second hydroxyl population because the characteristic H–O–H bending mode is still present at 1590 cm^{-1} , albeit very weak. At this low water content, this water must be present in the first monolayer.

In addition to the water and hydroxyl peaks, sharp peaks begin to emerge in the $0 - 800\text{ cm}^{-1}$ region. By comparison to the fully dehydrated sample, Figure 3h, and a low resolution literature spectrum [36], these are assigned to bulk phonons of RuO_2 . This is confirmed by the comparison with the calculated INS spectrum of RuO_2 , Figure 5, which is based on the ambient pressure neutron diffraction study of rutile RuO_2 [37]. The patterns of intensity are in reasonable agreement, although the highest energy modes are calculated to be too hard. Previous work [36] has shown that a LDA functional provides a better description in this instance, rather than the GGA PBE functional used here.

TGA and DTA, Figure 6, shows that there are two major weight loss events, one occurs around $100\text{ }^\circ\text{C}$ and corresponds to the loss of water seen in the INS spectra on heating the as received sample to $100\text{ }^\circ\text{C}$, Figure 3b and c, the second occurs around

330 °C. This accounts for why the INS spectra of the samples with $0.99 \geq x \geq 0.46$ are similar: they are all prepared below where the second weight loss occurs.

This also helps explain why the optimal material has $x = 0.5 - 0.7$ [22], in this range the surface structure is stable and minor variations in composition will not affect the specific capacitance.

DFT calculations [38] show that the energies of the bridging-oxygen terminated RuO_2 (110), $\text{RuO}_2(100)$ and $\text{RuO}_2(101)$ surfaces are: $71 \text{ meV } \text{\AA}^{-2}$, $87 \text{ meV } \text{\AA}^{-2}$ and $76 \text{ meV } \text{\AA}^{-2}$ respectively, hence the predominant facet in polycrystalline RuO_2 is expected to be the (110) face. The clean surface consists of rows of bridging oxygen atoms and coordinatively unsaturated ruthenium sites (Ru-cus) [38], Figure 7a. Surface science studies of single crystal RuO_2 (110) surfaces show that addition of O_2 results in the addition of an O atom to the Ru-cus [39], addition of H_2 causes protonation of the bridging oxygen and generation of water at oxygen that is adsorbed on the Ru-cus [40,41]. Addition of water results in molecular water being adsorbed at the Ru-cus [42]. Electrochemical measurements [43] suggest that a mixture of water and hydroxyls are present depending on the applied potential.

While the surface science investigations provide insights into the species likely to be present at the surface, the material used here is a nanocrystalline powder synthesised in aqueous solution [44,45]. To gain insight into the likely surface structures, we have investigated computationally a range of possible structures. These are described in Table S1 and Figures S1-S9 of the Supplementary Material. In all cases where imaginary modes were obtained, they were significant, $>|50| \text{ cm}^{-1}$, and involved proton motion, indicating that the structure is not viable. Typically, these involved higher symmetry structures, *e.g.* if a bridging oxygen was converted to a bridging

hydroxyl, or if the hydrogen was oriented vertically, it gave imaginary modes, whereas if it was tilted, all real modes were obtained, cf. Figures S1 and S2.

Comparison of observed and calculated INS spectra is a stringent test of a model [46]. From the modelling several clear conclusions emerge. Structures with water present, invariably resulted in too much intensity in the 250 – 750 cm^{-1} region (Figures S4, 5-7, 9). Structures with singly or doubly protonated O-bridge resulted in poor agreement (Figures S1, S2, S4-S7). The model that showed the best agreement is shown in Figure 7b (the comparison of observed and calculated spectra are shown in Figure 8a,b) and consists of hydrogen-bonded Ru–O–H oriented along [001] *i.e.* parallel to O-bridge.

From the results of the modelling, and in particular Figure 8, the best agreement between experiment and theory is obtained for a model where the surface is largely hydroxylated with, at most, small amounts of water present. This result necessitates a re-assignment of the spectra in Figure 3c-g. The peaks at 475 and 935 cm^{-1} are now assigned as the in-plane and out-of-plane Ru–O–H bending modes respectively. The broad feature at 65 – 300 cm^{-1} has contributions from O–Ru–O bending modes in the bulk, but is mostly due to the in-plane (220 cm^{-1}) and out-of-plane (90 cm^{-1}) O–Ru–OH bending modes. The Ru–OH stretch is calculated at 594 cm^{-1} but is hidden by the deformation modes. The only feature unaccounted for is the mode at 1605 cm^{-1} . This may be the combination mode: (in-plane + out-of-plane Ru–O–H bending modes) but it is more likely that it is a residual water contribution. Adding a hydrogen-bonded water molecule to the model shown in Figure 7b, generates that shown in Figure 7c and Figure 8c. As stated earlier, the intensity in the 250 – 750 cm^{-1} region is too strong, indicating that there is much less than a monolayer of water present. The presence of water is confirmed by the spectrum in the O–H stretch region, Figure 4c, which shows a

peak at 3600 cm^{-1} , assigned to the O–H stretch of the hydroxyls, and a weak broad peak centred at $\sim 3200\text{ cm}^{-1}$, which is similar in shape and position to that of the water in the parent material, Figure 4b.

Conclusions

The combination of neutron scattering studies and DFT calculations have provided new insight into the nature of the surface species present on $\text{RuO}_2 \cdot x\text{H}_2\text{O}$. Our results confirm that hydrous ruthenium oxide is a nanocrystalline material consisting of a core of rutile RuO_2 . We show for the first time that the surface consists largely of Ru–OH with small amounts of water hydrogen-bonded to the surface, *i.e.* hydrous ruthenium oxide is a core-shell material. The hydroxyls are stable up to $\sim 200\text{ }^\circ\text{C}$, over the composition range $x = 0.2 - 2$.

Hydrous ruthenium oxide is a mixed electronic-protonic conductor [21]. RuO_2 is a metallic conductor, accounting for the electronic conductivity. The charge storage mechanism is explained by the “double insertion” of electrons and protons into the structure:



The optimal supercapacitor material has $x = 0.5 - 0.7$ [22], and in this range the surface is fully hydroxylated. This provides an easy route for the proton transport: a proton can attach to a surface hydroxyl to generate coordinated water, proton transport then occurs along the hydrogen-bonded chain (Figure 7b) by a Grotthuss mechanism.

Acknowledgements

The STFC Rutherford Appleton Laboratory is thanked for access to neutron beam facilities. Computing resources (time on the SCARF compute cluster for the CASTEP calculations) was provided by STFC's e-Science facility.

Declaration of interest statement

The authors declare that there are no competing interests.

References

- [1] M Jayalakshmi, and K Balasubramanian, *J. Electrochem. Sci.* **3**, 1196 (2008).
- [2] Z.S. Iro, C. Subramani, and S.S. Dash, *Int. J. Electrochem. Sci.* **11**, 10628 (2016).
- [3] P.Y. Chan, and S.R. Majid, in *Advanced Materials and their Applications - Micro to nano scale*, Eds. I. Ahmad, P. Di Sia, and R. Raza, (One Central Press, Altrincham, 2017), ch. 2, pp 123-30.
- [4] Y. Wang, Z. Shi, Y. Huang, Y. Ma, C. Wang, M. Chen and Y. Chen, *J. Phys. Chem. C* **113**, 13103 (2009).
- [5] J.R. Miller, and P. Simon, *Science* **321**, 651 (2008).
- [6] A.G. Pandolfo, and A.F. Hollenkamp, *J. Power Sources* **157**, 11 (2006).
- [7] C.-C. Hu, K.-H. Chang, M.-C. Lin, and Y.-T. Wu, *Nano Lett.* **6**, 2690 (2006).
- [8] W.-C. Fang, J.-H. Huang, L.-C. Chen, Y.-L. O. Su, K.-H. Chen, *J. Power Sources* **160**, 1506 (2006).
- [9] K.-H. Chang, C.-C. Hu, and C.-Y. Chou, *Chem. Mater.* **19**, 2112-2119 (2007).
- [10] X. Wu, Y. Zeng, H. Gao, J. Su, J. Liu. and Z. Zhu, *J. Mater. Chem. A* **1**, 469 (2013).
- [11] Q. Li, S. Zheng, Y. Xu, H. Xue, and H. Pang, *Chemical Engineering Journal* **333**, 505–518 (2018).
- [12] C. Lin, J.A. Ritter, and B.N. Popov, *J. Electrochem. Soc.* **146**, 3155 (1999).
- [13] Y. Sato, K. Yomogida, T. Nanaumi, K. Kobayakawa, Y. Ohsawa, and M. Kawai, *Electrochem. Solid-State Lett.* **3**, 113-116 (2000).

- [14] C. Wang, and A.J. Appleby, *J. Electrochem. Soc.* **150**, A493 (2003).
- [15] S. Zhu, S. Wang, Y. Gao, L. Jiang, H. Sun, and G. Sun, *Int. J. Hydrogen Energy* **35**, 11254 (2010).
- [16] H. Yu, X. Fu, C. Zhou, F. Peng, H. Wang, and J. Yang, *Chem. Commun.*, 2408 (2009).
- [17] H. Yu, Y. Zhang, X. Fu, F. Peng, H. Wang, and J. Yang, *Catalysis Communications* **10**, 1752 (2009).
- [18] J.P. Zheng, and Y. Xin, *J. Power Sources* **110**, 86 (2002).
- [19] D.A. McKeown, P.L. Hagans, L.P.L. Carette, A.E. Russell, K.E. Swider, D.R. Rolison, *J. Phys. Chem. B* **103**, 4825 (1999).
- [20] W. Dmowski, T. Egami, K.E. Swider-Lyons, C.T. Love, and D.R. Rolison, *J. Phys. Chem. B* **106**, 12677 (2002).
- [21] W. Dmowski, T. Egami, K.E. Swider-Lyons, W.-F. Yan, S. Dai, and S.H. Overbury, *Z. Krist.* **222**, 617–624 (2007).
- [22] Z. Ma, J.P. Zheng, and R. Fu, *Chem. Phys. Lett.* **331**, 64 (2000).
- [23] A.K. Soper, RAL Technical Report, RAL-TR-2011–013, (2011).
- [24] D. Colognesi, M. Celli, F. Cilloco, R.J. Newport, S.F. Parker, V. Rossi-Albertini, F. Sacchetti, J. Tomkinson, and M. Zoppi, *Appl. Phys. A* **74** [Suppl.] S64–S66 (2002).
- [25] S.F. Parker, D. Lennon, and P.W. Albers, *Appl. Spec.* **65**, 1325-1341 (2011).
- [26] S.J. Clark, M.D. Segall, C.J. Pickard, P.J. Hasnip, M.J. Probert, K. Refson, and M.C. Payne, *Z. Krist.* **220**, 567 (2005).
- [27] J. Perdew, K. Burke and M. Ernzerhof, *Phys. Rev. Lett.* **77**, 3865 (1996).
- [28] A.M. Rappe, K.M. Rabe, E. Kaxiras and J.D. Joannopoulos, *Phys. Rev. B* **41**, 1227 (1990).

- [29] K. Refson, S.J. Clark, and P. R. Tulip, *Phys. Rev. B* **73**, 155114 (2006).
- [30] A.J. Ramirez-Cuesta, *Comp. Phys. Comm.* **157**, 226 (2004).
- [31] J. Li, *J. Chem. Phys.* **105**, 6733-6755 (1996).
- [32] S.F. Parker, K. Refson, A.C. Hannon, E. Barney, S.J. Robertson and P. Albers, *J. Phys. Chem. C* **114**, 14164–14172 (2010).
- [33] E. Spencer, B. Huang, S.F. Parker, A. Kolesnikov, N.L. Ross and B. Woodfield, *J. Chem. Phys.* **139**, 244705 (2013)..
- [34] H.-W. Wang, M.J. DelloStritto, N. Kumar, A.I. Kolesnikov, P.R.C. Kent, J.D. Kubicki, D.J. Wesolowski, and J.O. Sofo, *J. Phys. Chem. C* **118**, 10805–10813 (2014).
- [35] D. Lennon, and S.F. Parker, *Acc. Chem. Res.* **47**, 1220-1227 (2014).
- [36] K.-P. Bohnen, R. Heid, O. de la Peña Seaman, B. Renker, P. Adelmann, and H. Schober, *Phys. Rev. B* **75**, 092301 (2007).
- [37] J. Haines, J. M. Léger, O. Schulte, and S. Hull, *Acta Cryst.* **B53**, 880-884 (1997).
- [38] H. Over, Y.D. Kim, A.P. Seitsonen, S. Wendt, E. Lundgren, M. Schmid, P. Varga, A. Morgante, and G. Ertl, *Science* **287**, 1474-1476 (2000).
- [39] Y.D. Kim, A.P. Seitsonen, S. Wendt, J. Wang, C. Fan, K. Jacobi, H. Over, and G. Ertl, *J. Phys. Chem. B* **105**, 3752-3758 (2001).
- [40] K. Jacobi, Y. Wang, and G. Ertl, *J. Phys. Chem. B* **110**, 6115-6122 (2006).
- [41] M. Knapp, D. Crihan, A. P. Seitsonen, E. Lundgren, A. Resta, J. N. Andersen, and H. Over, *J. Phys. Chem. C* **111**, 5363-5373 (2007).
- [42] A. Lobo, and H. Conrad, *Surf. Sci.* **523**, 279–286 (2003).
- [43] Y.S. Chu, T.E. Lister, W.G. Cullen, H. You, and Z. Nagy, *Phys. Rev. Lett.* **86**, 3364-3367 (2001).

- [44] J.P. Zheng, P.J. Cygan, and T.R. Jow, *J. Electrochem. Soc.* **142**, 2699-2703 (1995).
- [45] K.-H. Chang, C.-C. Hu, and C.-Y. Chou, *Chem. Mater.* **19**, 2112-2119 (2007).
- [46] G.J. Kearley, and M.R. Johnson, *Vib. Spec.* **53**, 54–59 (2010).

Table 1. The samples used and their preparation conditions.

Preparation conditions	x in $\text{RuO}_2 \cdot x\text{H}_2\text{O}$	
	Gravimetric	TGA
Dried at 500 °C for 65 hours.	0.00	0.01
Dried at 300 °C for 22 hours.	0.12	—
Dried at 190 °C for 22 hours.	0.46	0.54
Dried at 169 °C for 23 hours.	0.53	0.69
Dried at 150 °C for 18 hours.	0.63	0.80
Dried at 100 °C for 22 hours.	0.99	1.27
Used as received.	2.02	1.77

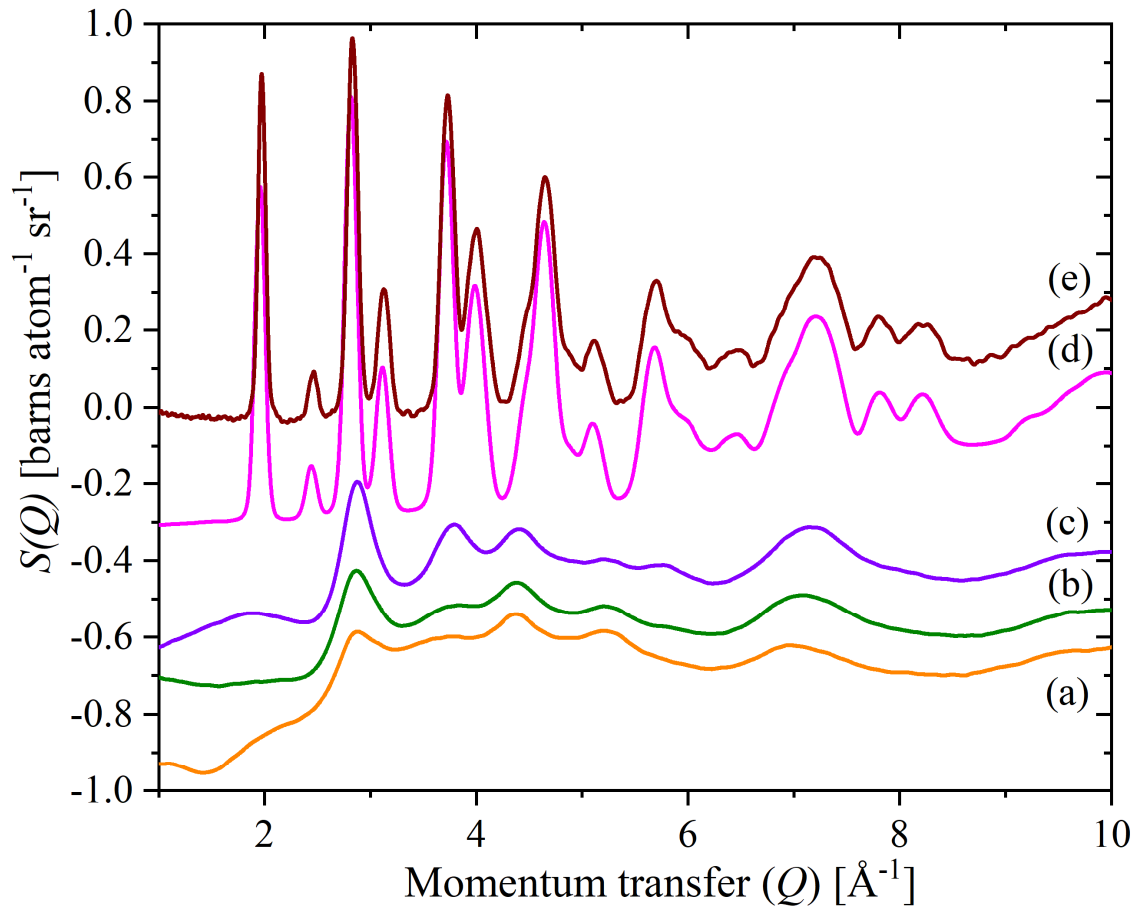


Figure 1. Neutron diffraction patterns of $\text{RuO}_2 \cdot x\text{H}_2\text{O}$. (a) $x = 2.02$, (b) $x = 0.63$, (c) $x = 0.43$, (d) $x = 0$ and (e) reference anhydrous RuO_2 .

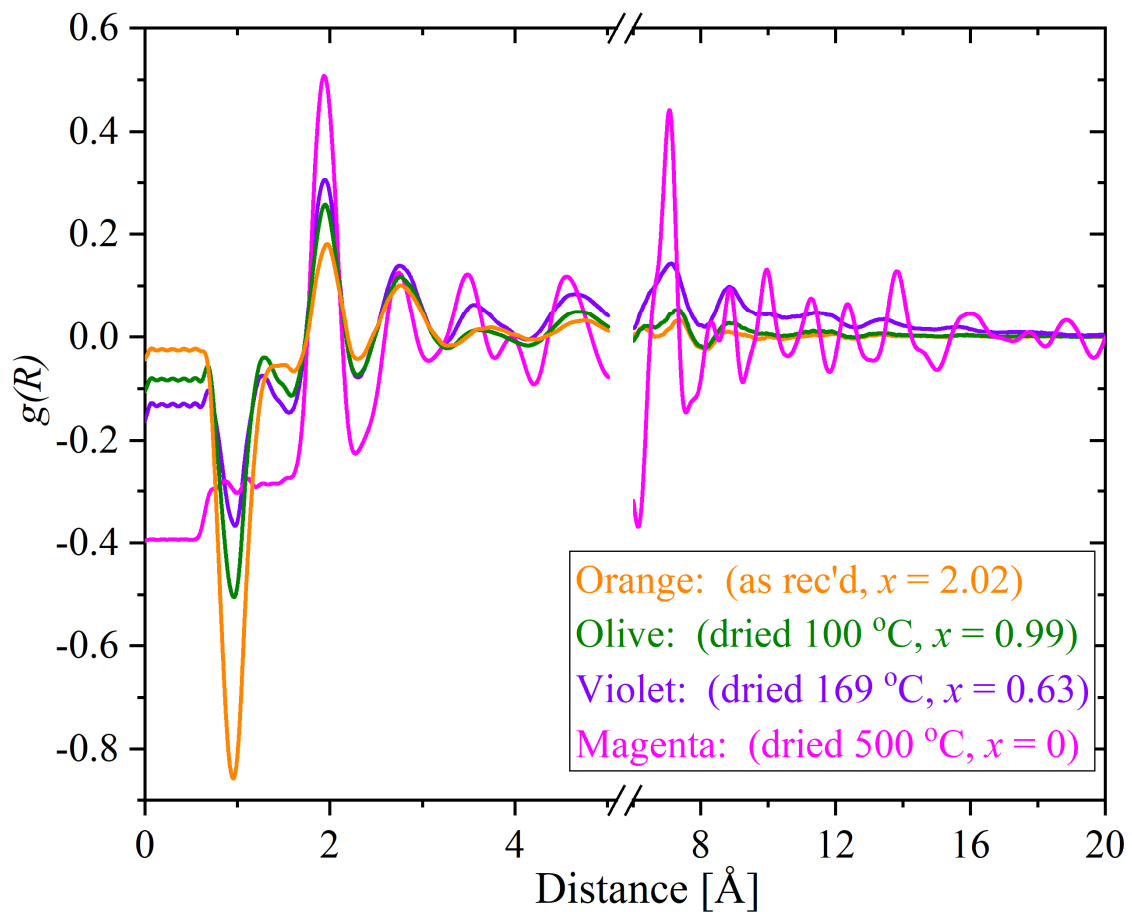


Figure 2. Radial distribution functions for $\text{RuO}_{2 \cdot x}\text{H}_2\text{O}$. The ordinate scale for the 6 – 20 Å region is $\times 3$ that of the 0 – 5 Å region.

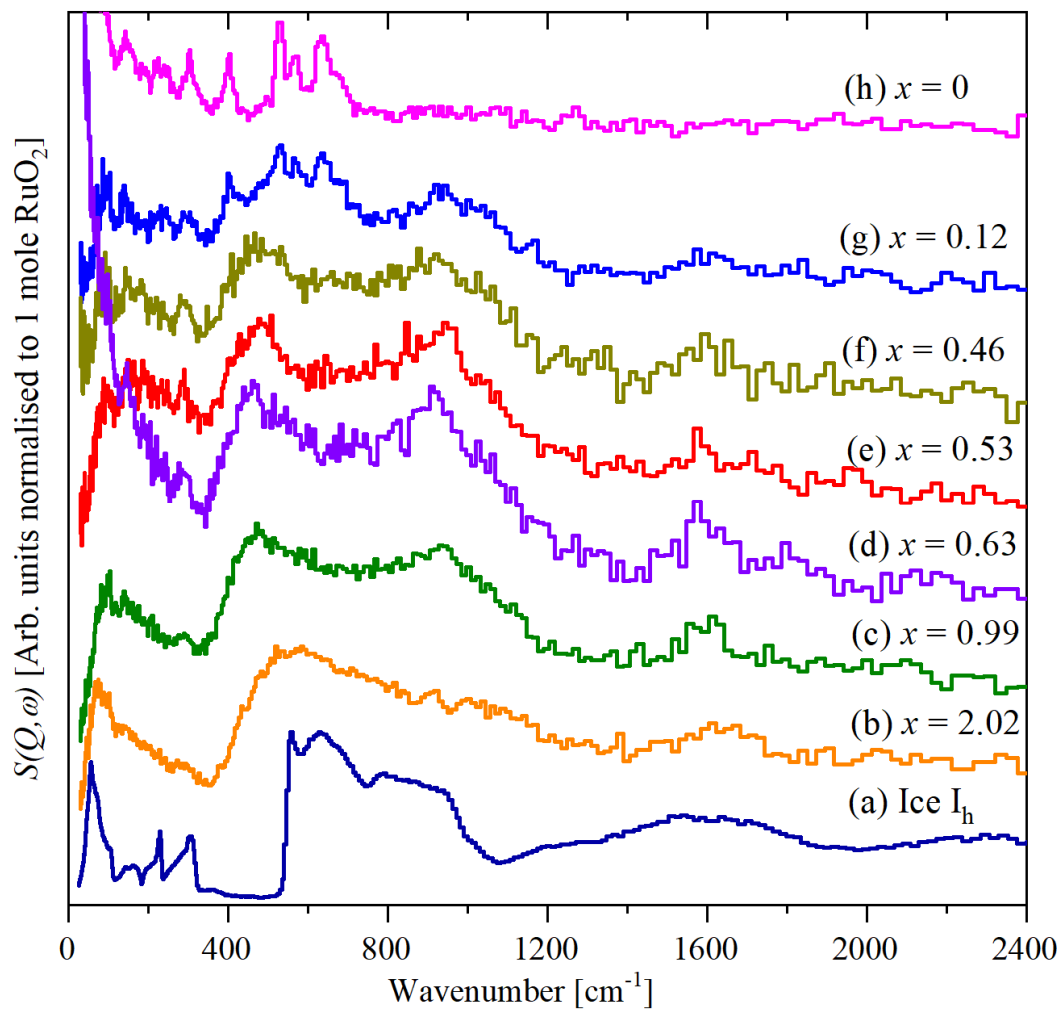


Figure 3. INS spectra of $\text{RuO}_2 \cdot x\text{H}_2\text{O}$. Relative to (a): (c) is $\times 2$, (d), (e) and (f) are $\times 12$ and (g) and (h) are $\times 24$ ordinate scale expanded.

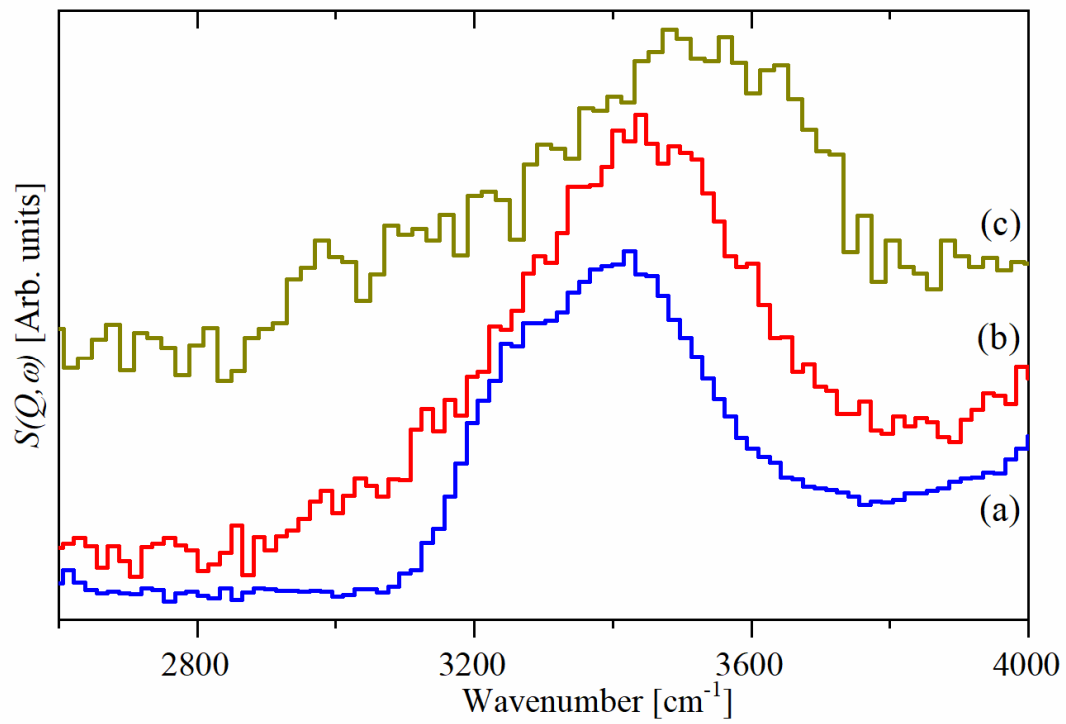


Figure 4. INS spectra in the O–H stretch region of: (a) ice I_h , (b) $\text{RuO}_2 \cdot 2.85\text{H}_2\text{O}$ and (c) $\text{RuO}_2 \cdot 0.43\text{H}_2\text{O}$. (c) is ordinate expanded $\times 20$ relative to (b).

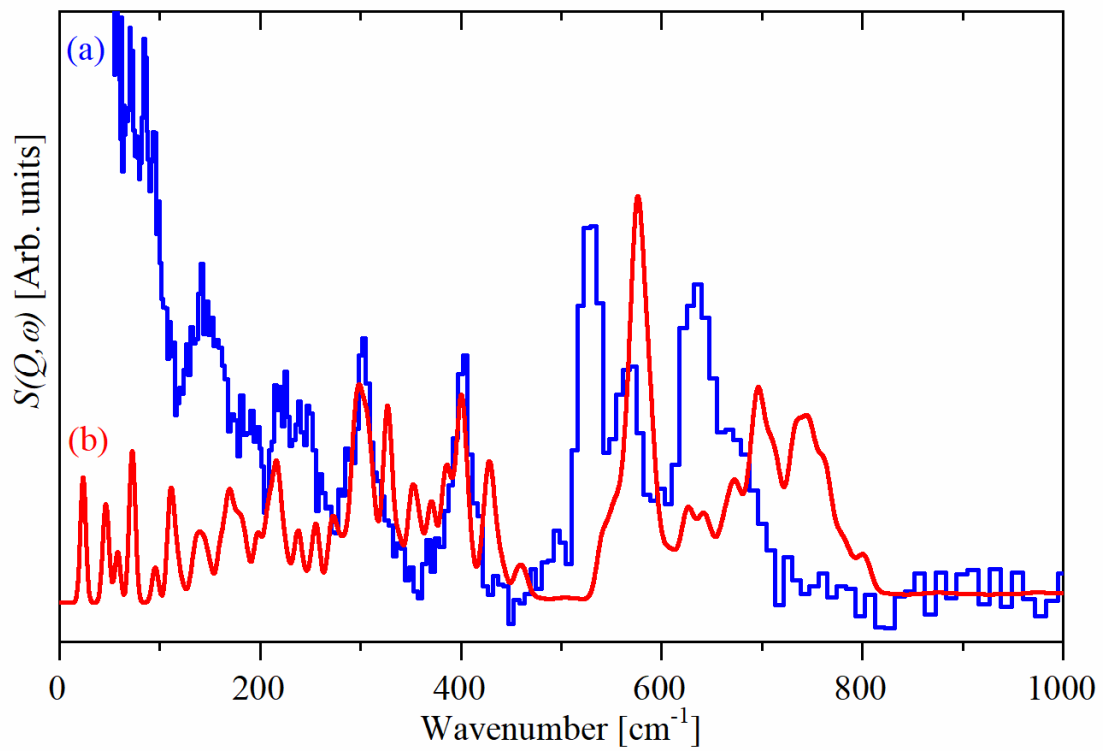


Figure 5. Comparison of: (a) the INS spectrum of RuO₂ and (b) that calculated by DFT.

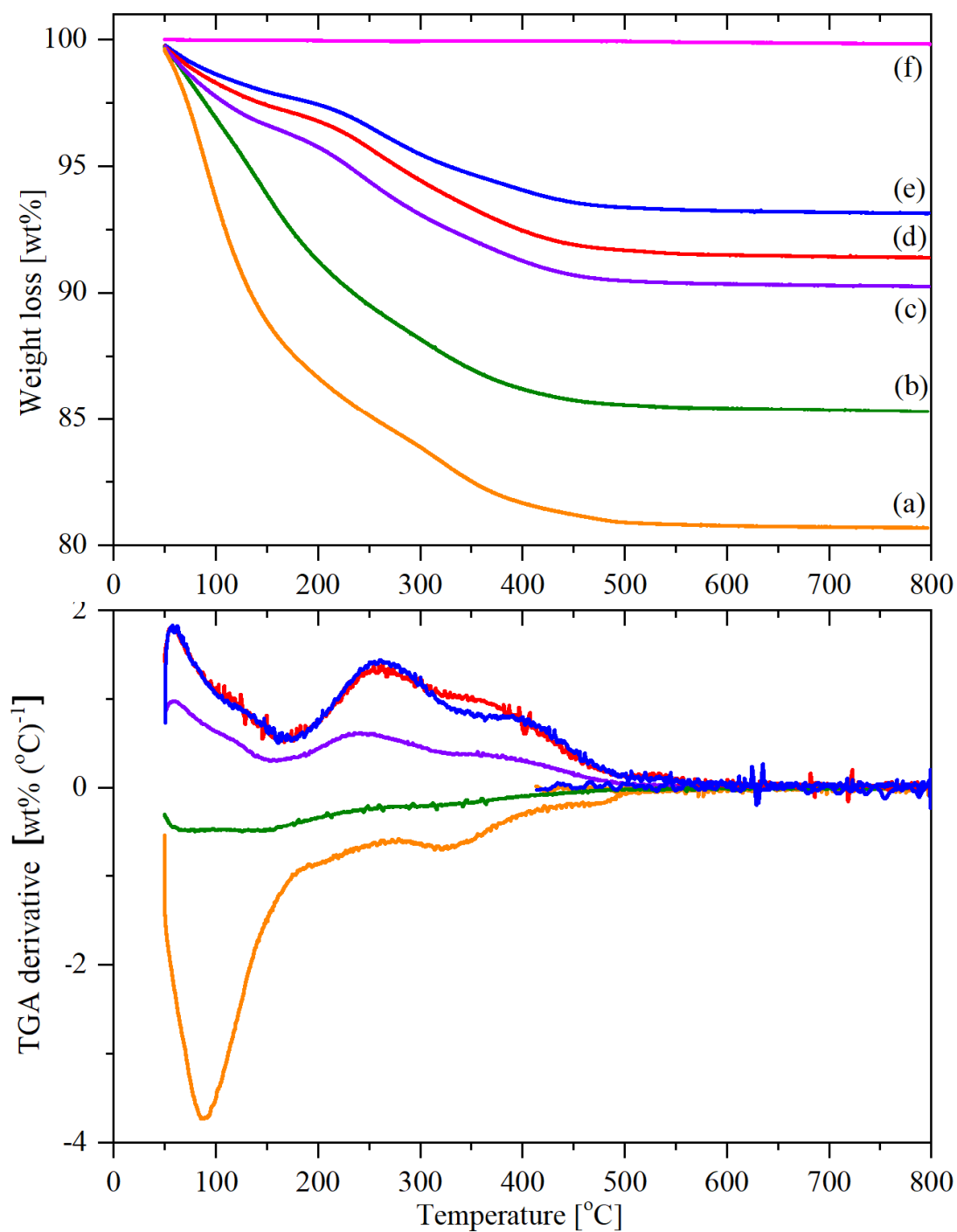


Figure 6. Top part: TGA data for $\text{RuO}_2 \cdot x\text{H}_2\text{O}$ dried at: (a) as received $x = 2.02$, (b) 100 °C, $x = 0.99$, (c) 150 °C, $x = 0.63$, (d) 169 °C, $x = 0.53$, (e) 190 °C, $x = 0.46$, and (f) 500 °C, $x = 0$. The lower part is the first derivative of the TGA traces above, the colour code is the same in both cases, with the 500 °C sample omitted from the derivative traces.

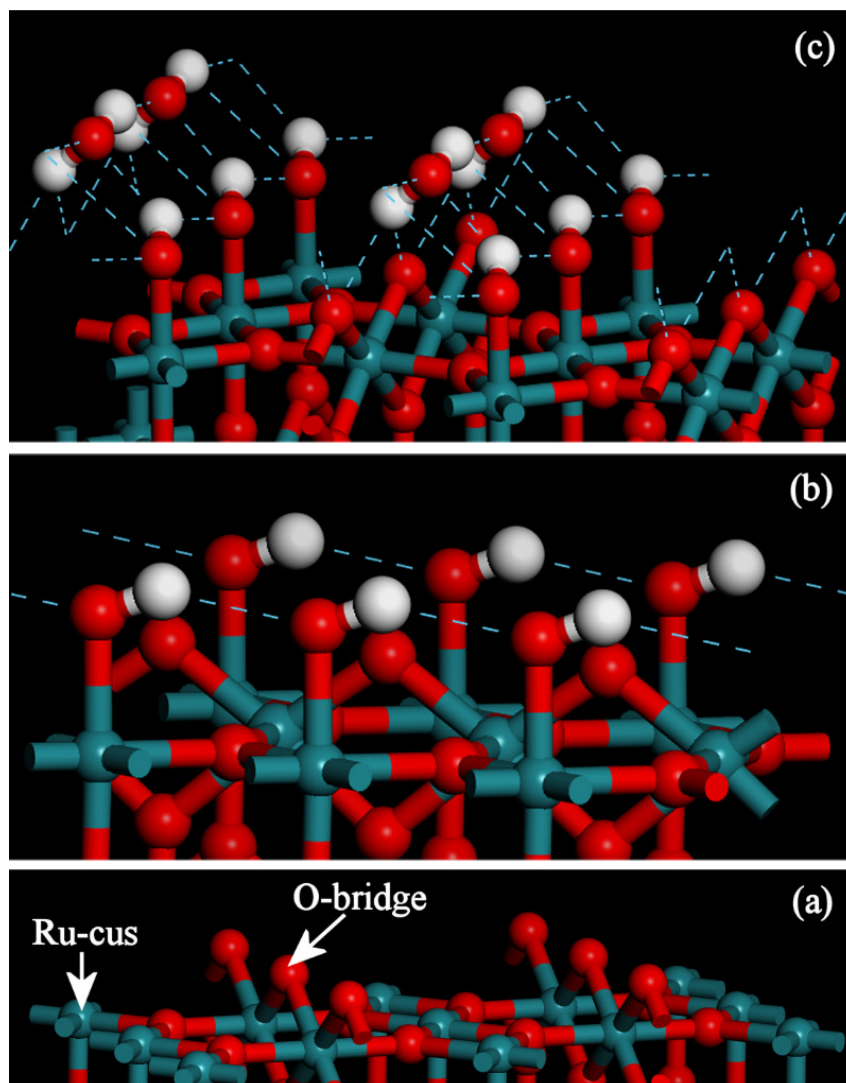


Figure 7. (a) The clean RuO₂ (110) surface showing the bridging oxygen atoms (O-bridge) and the coordinatively unsaturated ruthenium sites (Ru-cus), (b) the model that best accounts for the INS spectra and (c) same as (b) but with a water molecule hydrogen-bonded to the hydroxyls and the O-bridge. (Dark green = ruthenium, red = oxygen, white = hydrogen, dashed blue lines indicate hydrogen-bonds).

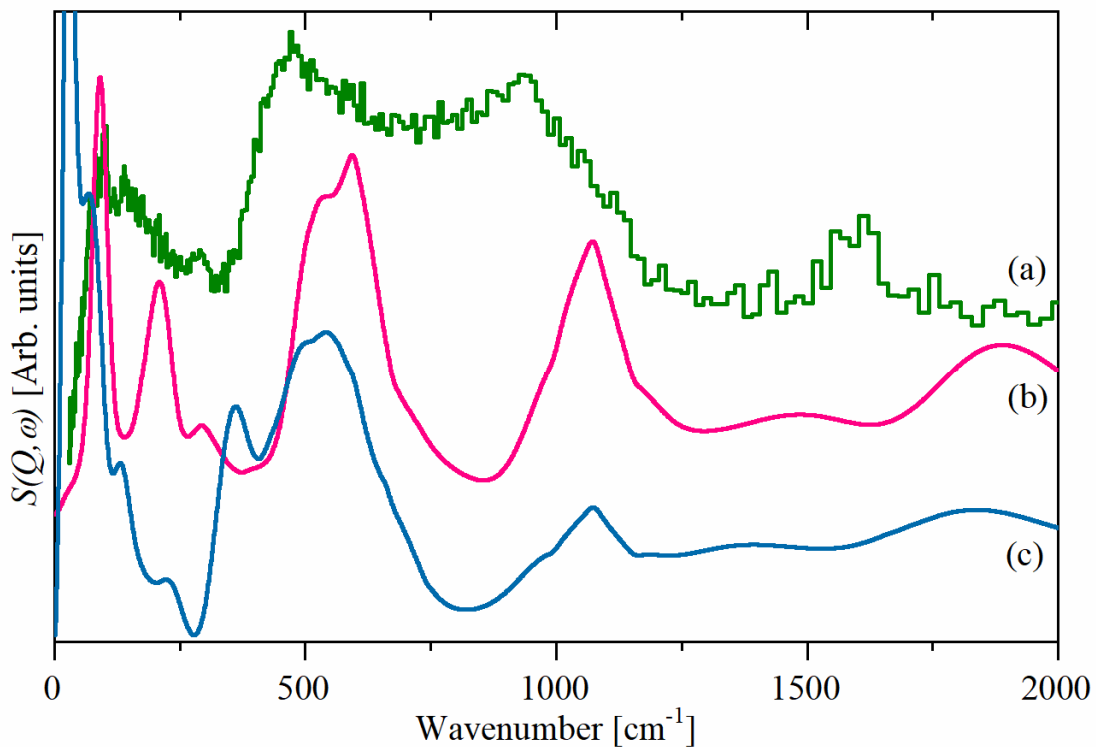


Figure 8. (a) INS spectrum of $\text{RuO}_2 \cdot 0.99\text{H}_2\text{O}$, (b) spectrum generated from the hydroxyls-only model shown in Figure 7b and (c) that generated from the hydroxyls-plus-water model shown in Figure 7c. In (b) and (c) the calculated modes have been broadened to mimic the disorder present on the surface. The resolution limited spectra are shown in Figures S8 and S9.

Electronic supplementary material for:

Structure and spectroscopy of the supercapacitor material hydrous ruthenium oxide, $\text{RuO}_2 \cdot x\text{H}_2\text{O}$, by neutron scattering

Stewart F Parker^{a*} Stephen J. Robertson^b and Silvia Imberti^a

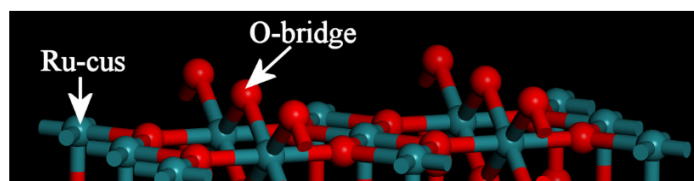
^a*ISIS Facility, STFC Rutherford Appleton Laboratory, Chilton, Didcot, OX11 0QX, UK*

^b*Advanced Material Group, STFC Rutherford Appleton Laboratory, Chilton, Didcot, Oxfordshire, OX11 0QX, UK*

E-mail: stewart.parker@stfc.ac.uk

Table S1 describes the various models of the surface species on RuO₂(110), a comparison of the INS spectrum of RuO₂·0.99H₂O with that calculated from the models are shown in Figures S1 – S9. The model used is shown as an inset in each figure.

Table S1. Description of the surface structures investigated.



Model and Figure number	Sites occupied		Number of imaginary modes
	Ru-cus	O-bridge	
1	None	H vertical	2
2	None	H tilted	0
3	O–H H-bonded to O-bridge	None	0
4	O–H oriented along [001]	Doubly protonated to H ₂ O	2
5	H ₂ O	H vertical	6
6	H ₂ O	H tilted	0
7	Alternating H ₂ O and O–H oriented along [001] ^a	None	2
8	O–H oriented along [001]	None	0
9	O–H oriented along [001]	H ₂ O H-bonded to O-bridge and Ru–O–H	0

^a [001] is along the direction of O-bridge.

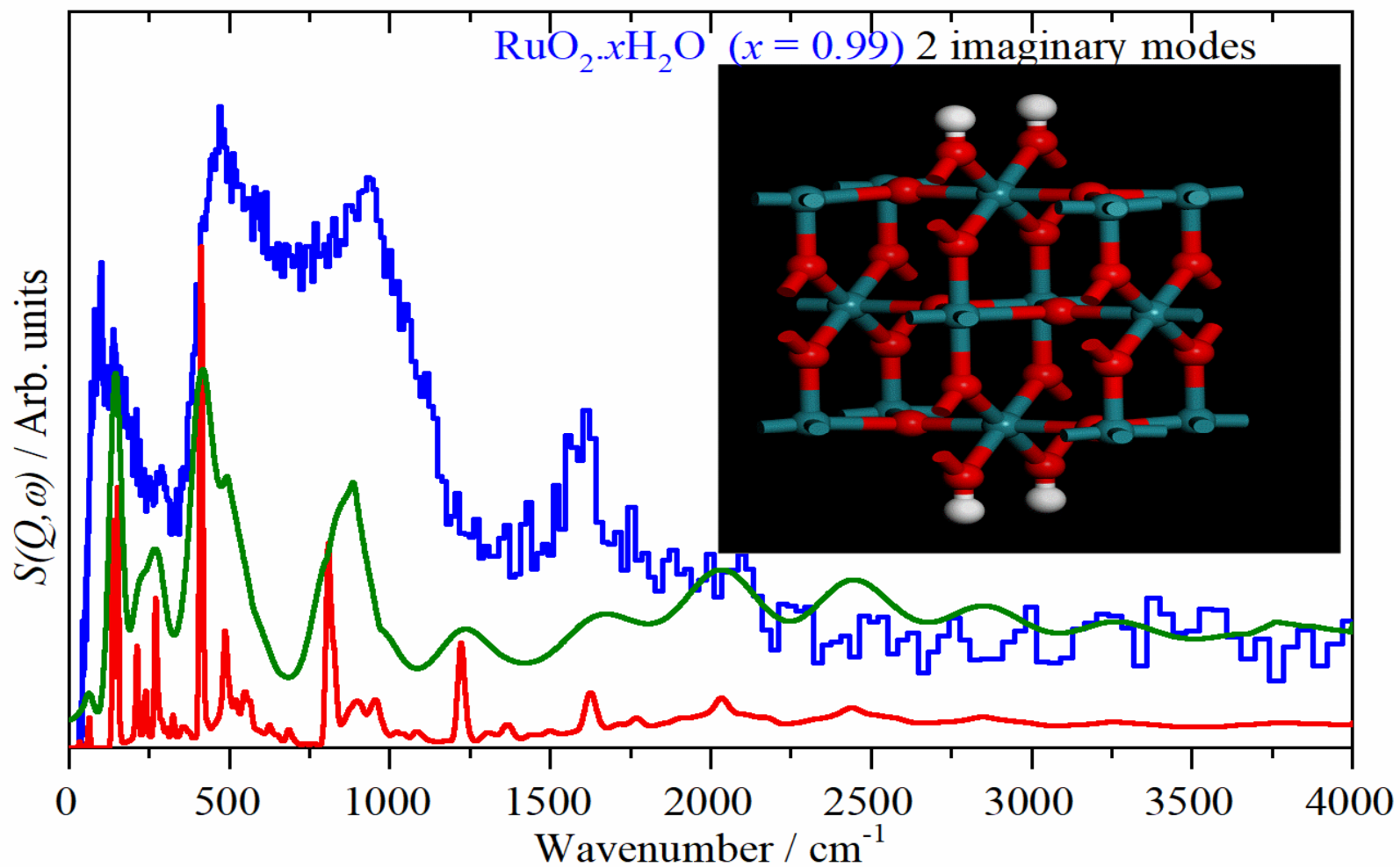


Figure S1. Blue trace: INS spectrum of $\text{RuO}_2 \cdot 0.99\text{H}_2\text{O}$, Red trace: INS spectrum calculated for calculated for Model 1 of the surface species present on Ru(110) (see Table S1 for details), Olive trace: as red trace but broadened to mimic surface disorder.

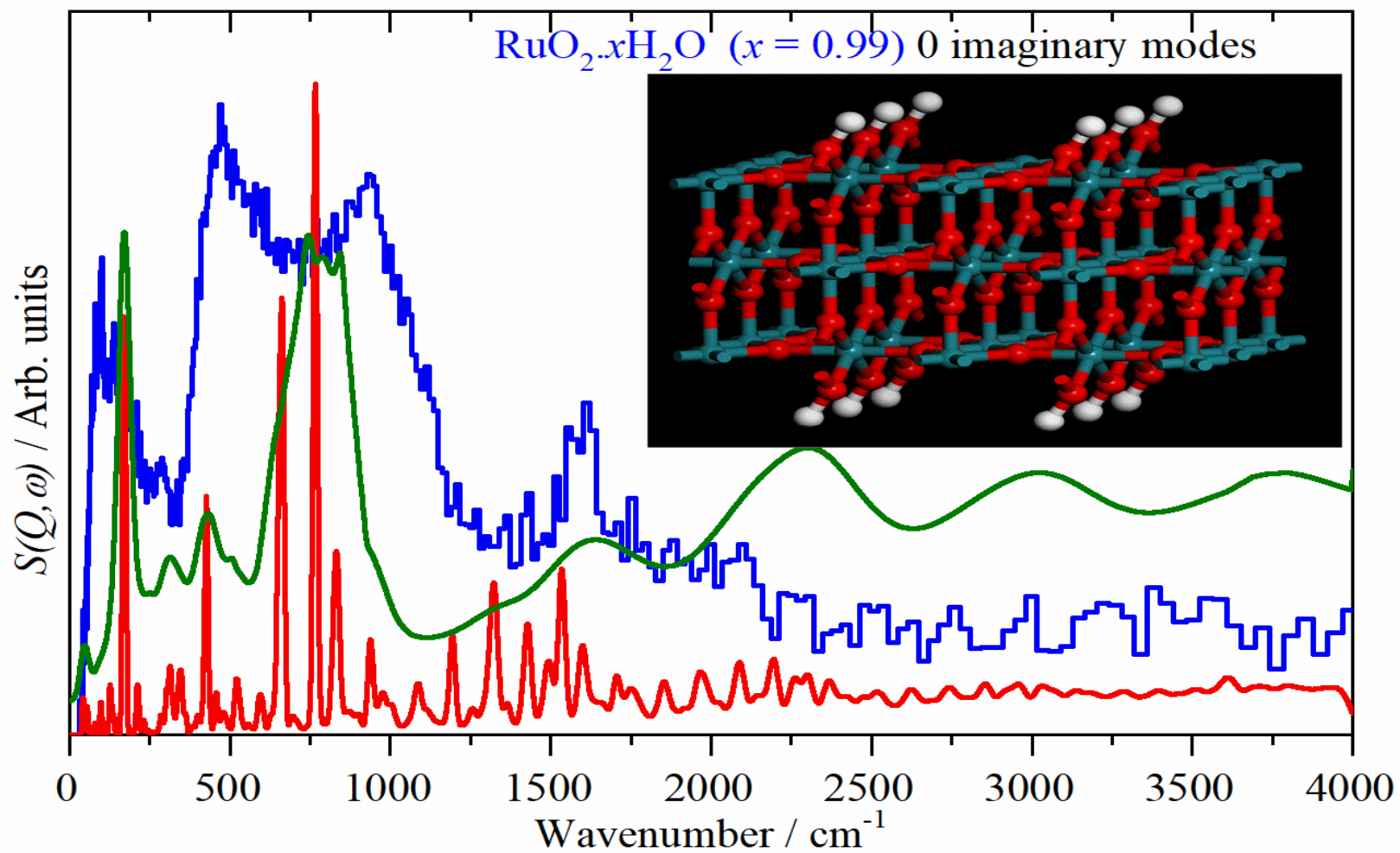


Figure S2. Blue trace: INS spectrum of $\text{RuO}_2 \cdot 0.99\text{H}_2\text{O}$, Red trace: INS spectrum calculated for calculated for Model 2 of the surface species present on Ru(110) (see Table S1 for details), Olive trace: as red trace but broadened to mimic surface disorder.

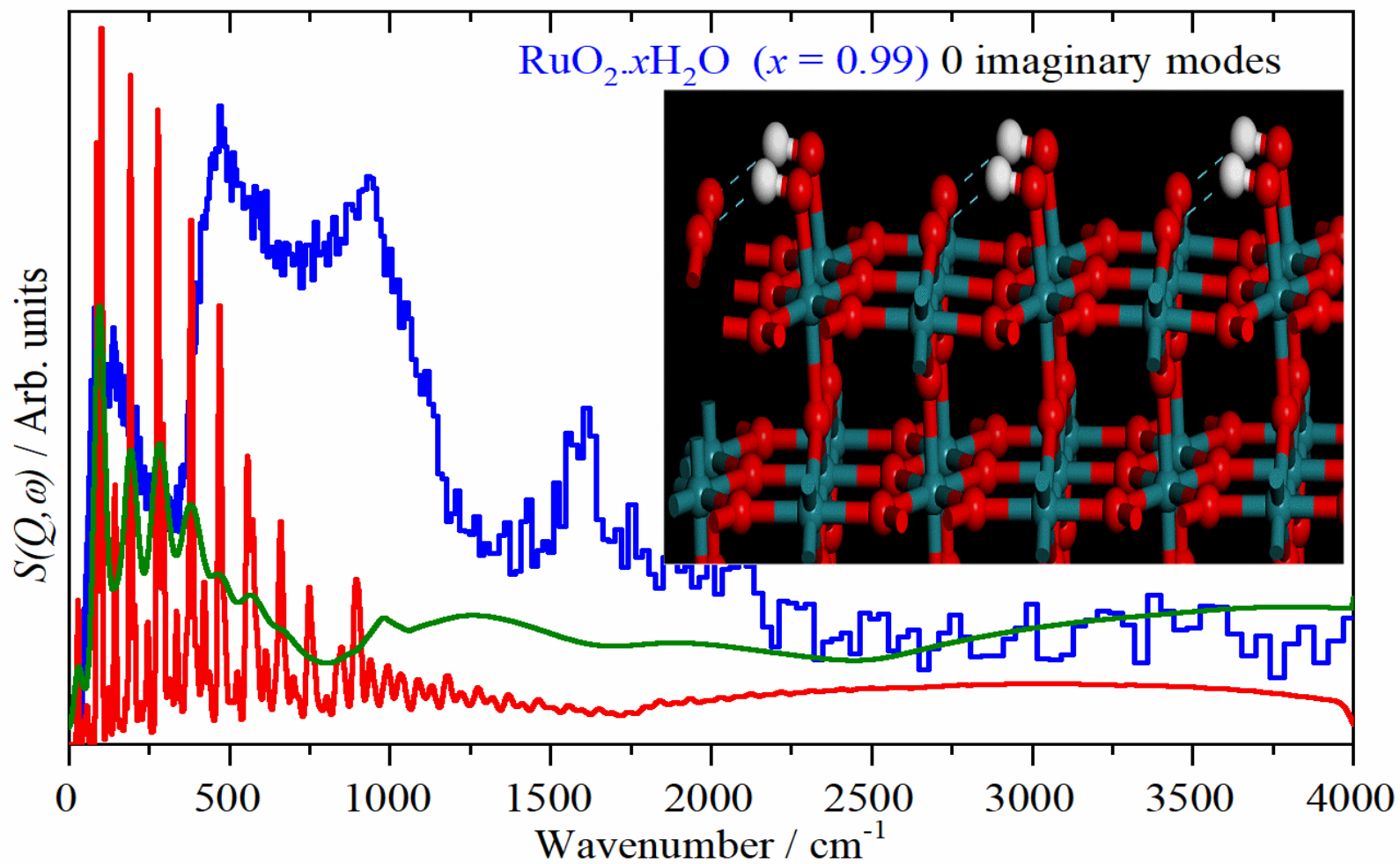


Figure S3. Blue trace: INS spectrum of RuO₂.0.99H₂O, Red trace: INS spectrum calculated for calculated for Model 3 of the surface species present on Ru(110) (see Table S1 for details), Olive trace: as red trace but broadened to mimic surface disorder.

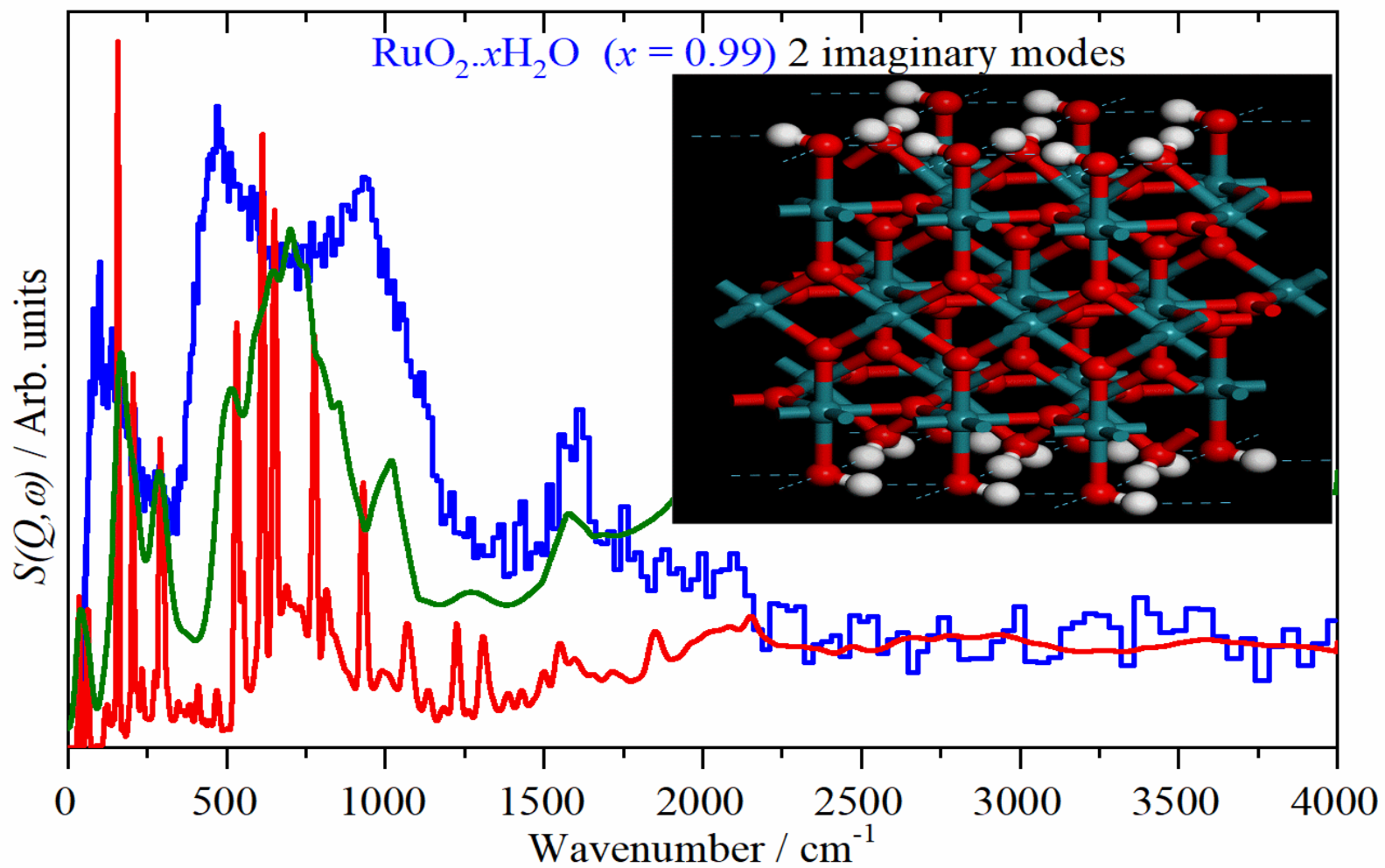


Figure S4. Blue trace: INS spectrum of $\text{RuO}_2 \cdot 0.99\text{H}_2\text{O}$, Red trace: INS spectrum calculated for Model 4 of the surface species present on Ru(110) (see Table S1 for details), Olive trace: as red trace but broadened to mimic surface disorder.

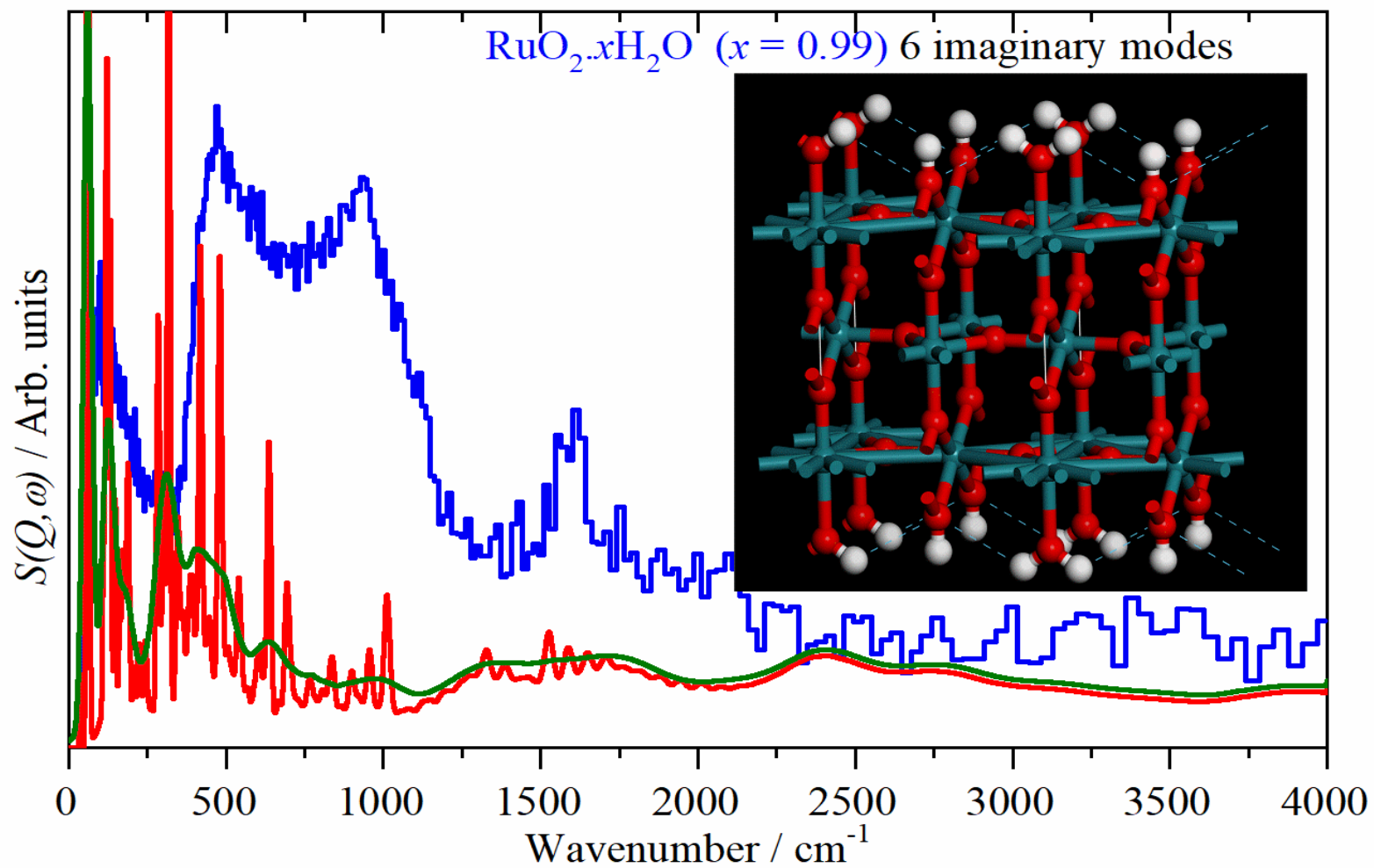


Figure S5. Blue trace: INS spectrum of RuO₂._{0.99}H₂O, Red trace: INS spectrum calculated for calculated for Model 5 of the surface species present on Ru(110) (see Table S1 for details), Olive trace: as red trace but broadened to mimic surface disorder.

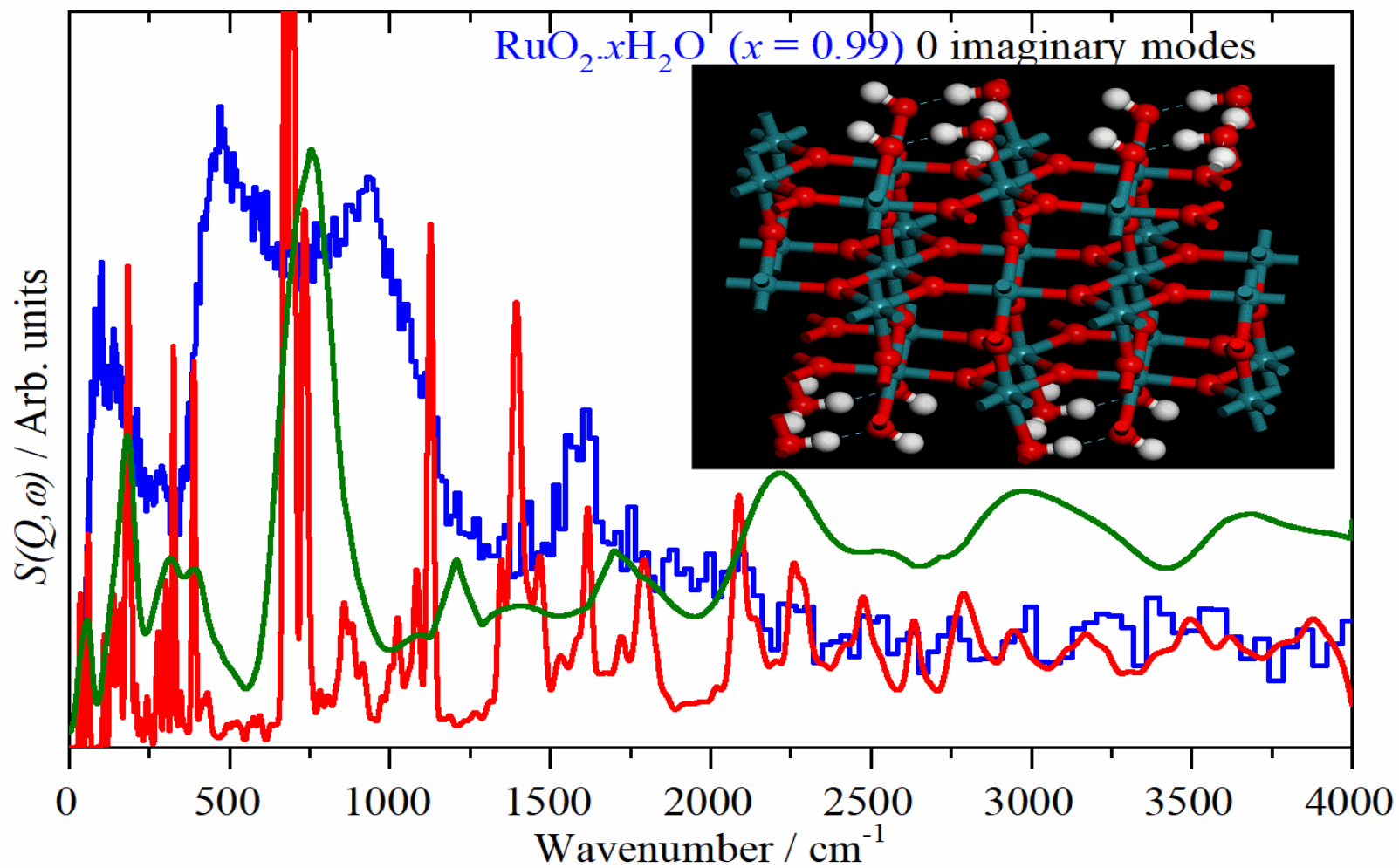


Figure S6. Blue trace: INS spectrum of $\text{RuO}_2 \cdot 0.99\text{H}_2\text{O}$, Red trace: INS spectrum calculated for Model 6 of the surface species present on Ru(110) (see Table S1 for details), Olive trace: as red trace but broadened to mimic surface disorder.

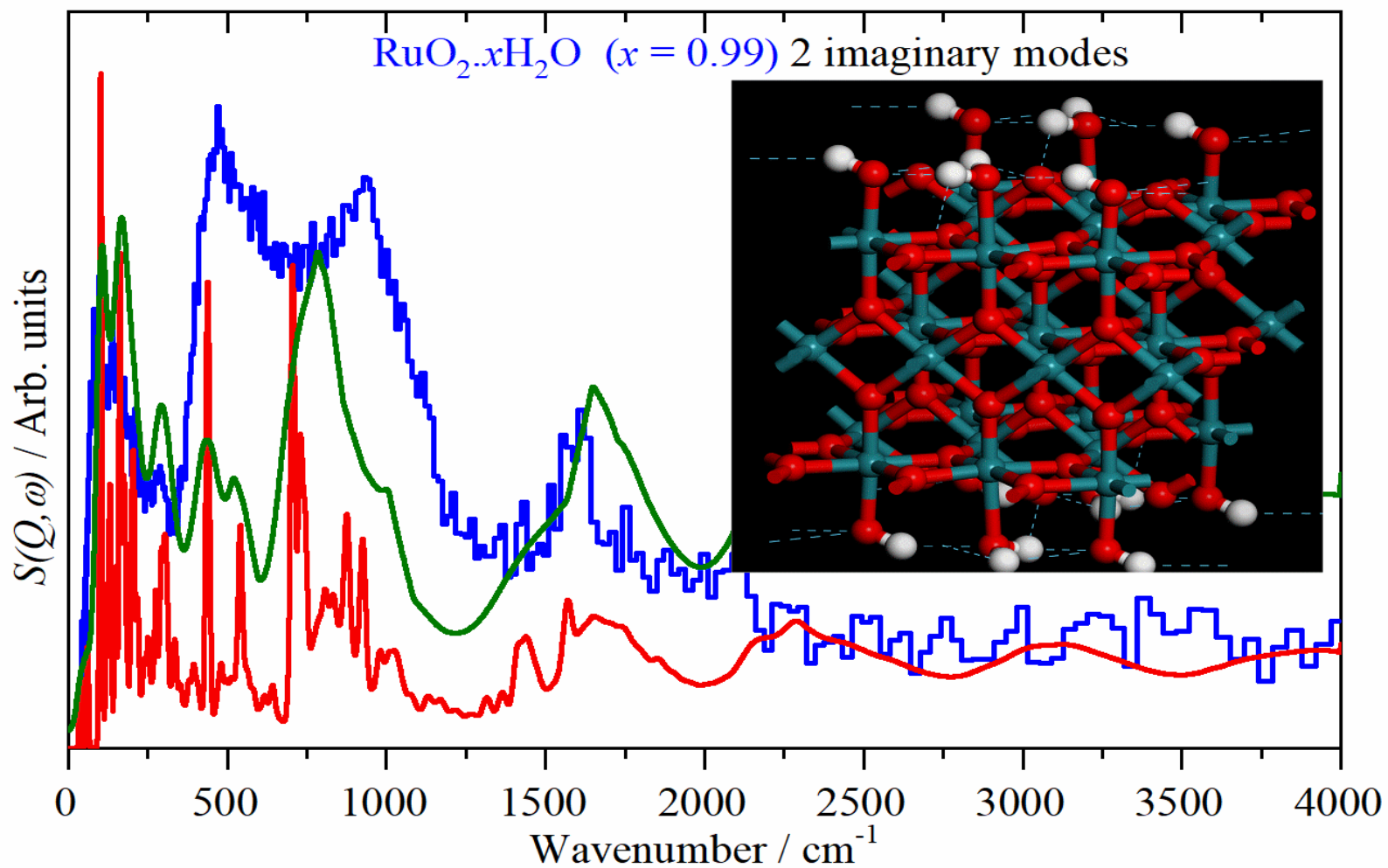


Figure S7. Blue trace: INS spectrum of $\text{RuO}_2 \cdot 0.99\text{H}_2\text{O}$, Red trace: INS spectrum calculated for calculated for Model 7 of the surface species present on Ru(110) (see Table S1 for details), Olive trace: as red trace but broadened to mimic surface disorder.

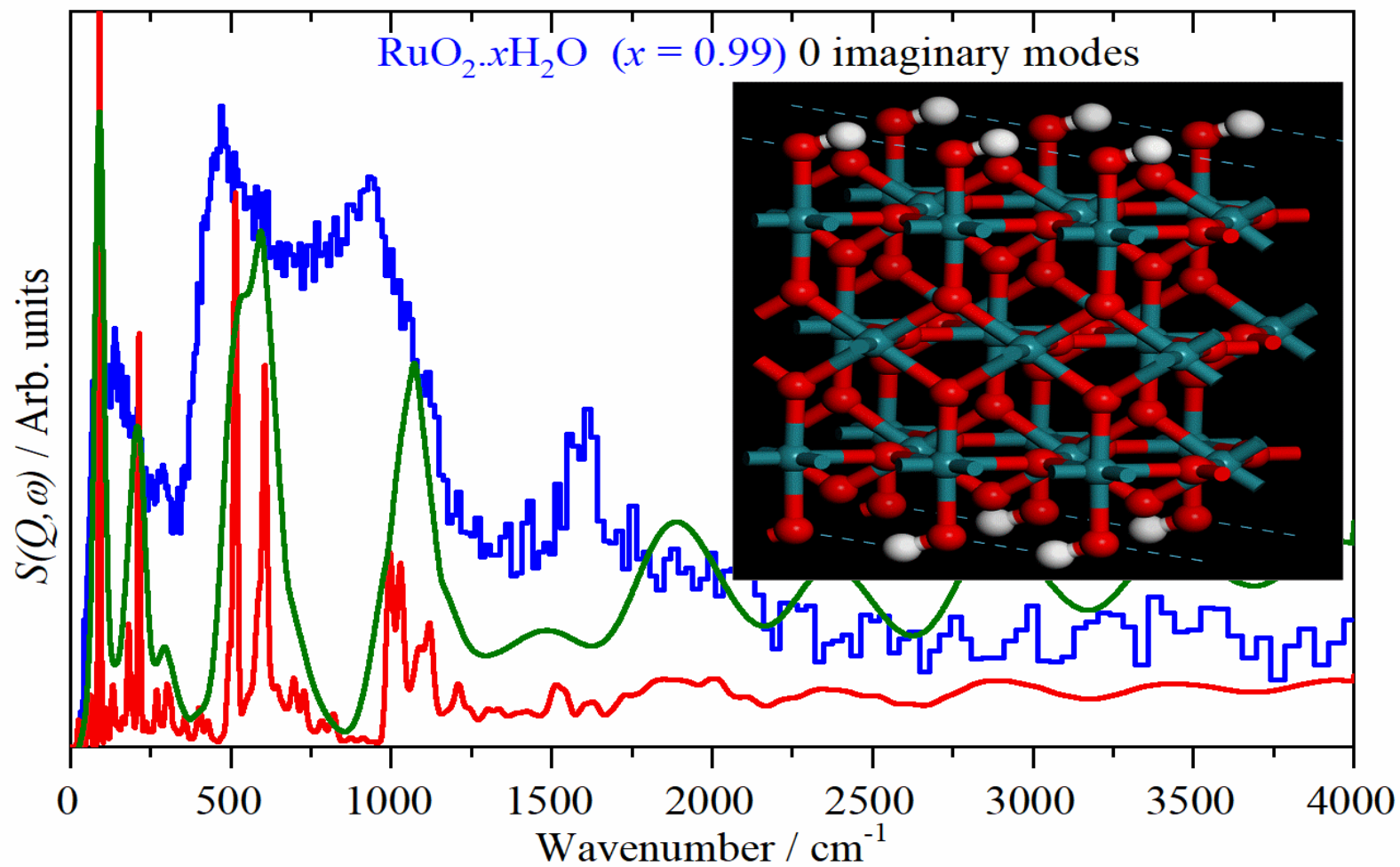


Figure S8. Blue trace: INS spectrum of RuO₂.0.99H₂O, Red trace: INS spectrum calculated for calculated for Model 8 of the surface species present on Ru(110) (see Table S1 for details), Olive trace: as red trace but broadened to mimic surface disorder.

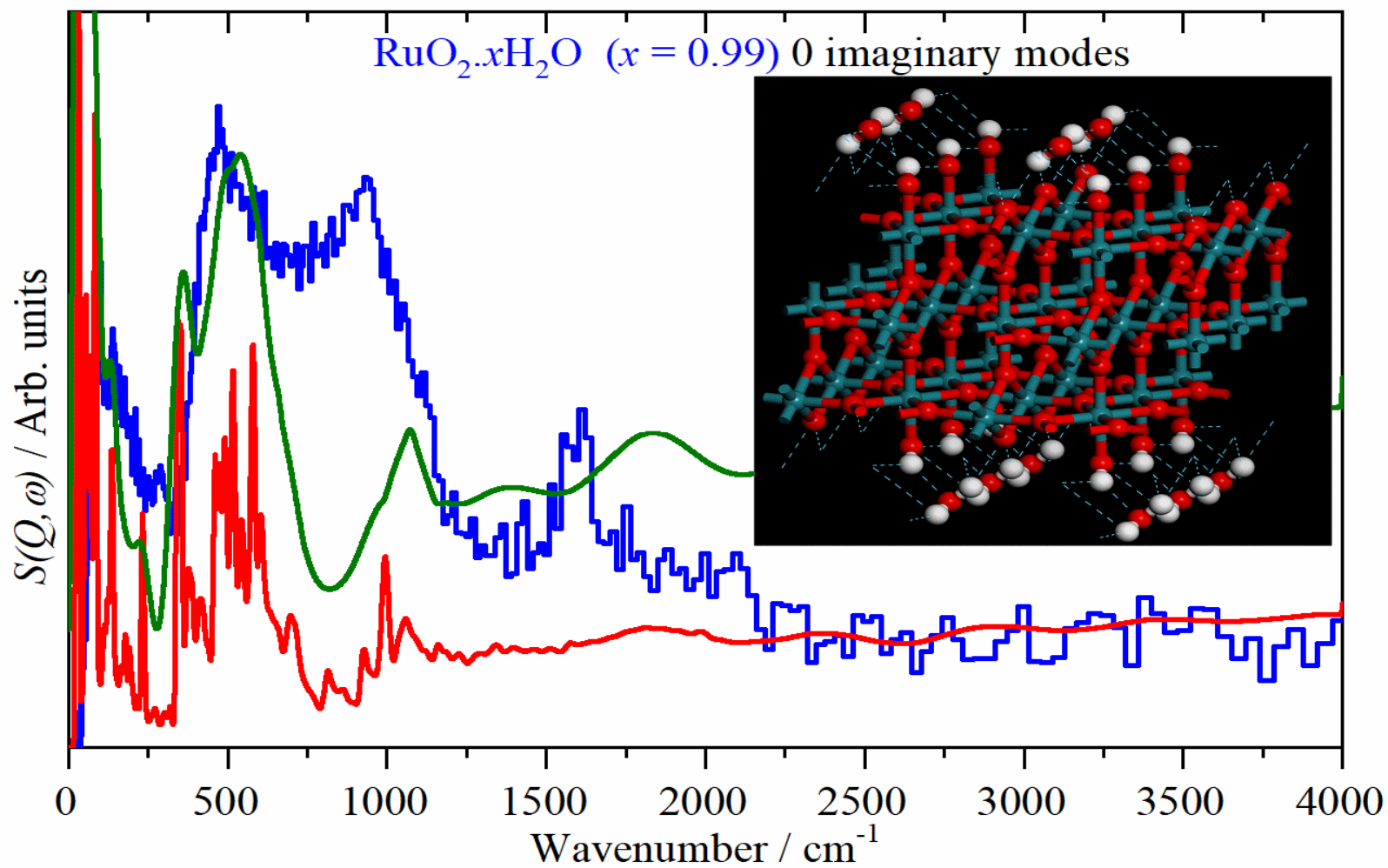


Figure S9. Blue trace: INS spectrum of RuO₂._{0.99}H₂O, Red trace: INS spectrum calculated for calculated for Model 9 of the surface species present on Ru(110) (see Table S1 for details), Olive trace: as red trace but broadened to mimic surface disorder.